

Fast lidar and radar multiple-scattering models

Part 1: Quasi-small-angle scattering using the photon variance-covariance method

ROBIN J. HOGAN*

Department of Meteorology, University of Reading, United Kingdom

Submitted to J. Atmos. Sci., October 2007

ABSTRACT

A fast, approximate method is described for the calculation of the intensity of multiply scattered lidar returns from clouds. At each range gate it characterizes the outgoing photon distribution by its spatial variance, the variance of photon direction and the covariance of photon direction and position. The result is that for an N -point profile the calculation is $O(N)$ efficient yet implicitly includes all orders of scattering, contrasting with the $O(N^m/m!)$ efficiency of models that explicitly consider each scattering order separately for truncation at m -order scattering. It is also shown how the shape of the scattering phase function near 180° may be taken into account for both liquid water droplets and ice particles. The model considers only multiple-scattering due to small-angle forward scattering events, which is suitable for most ground-based and airborne lidars due to their small footprint on the cloud. For spaceborne lidar, it must be used in combination with the wide-angle multiple scattering model described in Part 2 of this two-part paper.

1. Introduction

Lidar and radar have been used extensively from the ground to study clouds (Ackerman and Stokes 2003; Illingworth et al. 2007) but from space (Stephens et al. 2002; Winker et al. 2003) the interpretation of the backscattered signals is made more complicated by the much larger instrument footprints, which result in a greater fraction of the detected photons having undergone multiple scattering. It was shown by Hogan et al. (2006) that if consideration of lidar multiple-scattering effects are omitted in combined radar-lidar retrievals of ice clouds from space then the retrieved optical depth will be underestimated by around 40%. This two-part paper presents a new method for modeling such returns that is fast enough to be incorporated as a forward model in cloud retrieval schemes (e.g. Donovan et al. 2001; Delanoë and Hogan 2007).

By way of an introduction to the problem of multiple scattering, we consider the four scattering regimes that may be experienced by active remote sensors; a similar taxonomy was provided by Nicolas et al. (1997) but only for lidar. The regimes are shown schematically in Fig. 1 and are as follows:

0. No attenuation. The trivial case occurs when the optical depth of a medium $\delta \ll 1$, and the apparent backscatter $\hat{\beta}$ (or in the case of radar, the apparent radar reflectivity factor \hat{Z}) is equal to the “true” backscatter of the medium β (or Z) and can be interpreted unambiguously. This is the case for lidar observations of thin aerosol layers, mm-wave radar observations of ice clouds and cm-

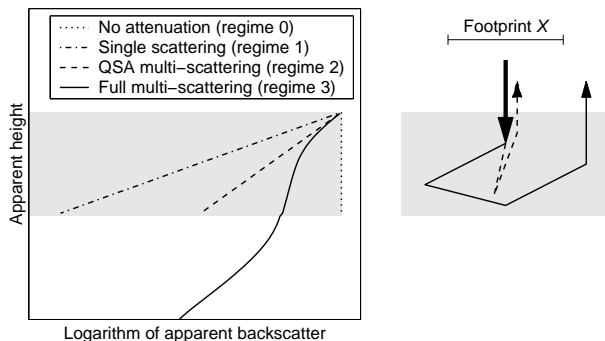


FIG. 1: Depiction of the four scattering regimes that active sensors encounter, as discussed in the text. The axes on the left indicate the apparent backscatter that a nadir-looking instrument would observe in a homogeneous slab of cloud in each of the four regimes. The schematic on the right depicts the nadir beam entering the cloud (thick arrow), with the dashed arrow showing the trajectory of a photon subject to a quasi-small-angle (QSA) forward scattering event on both the outgoing and return journey, but only one large-angle scattering event. The thin solid arrow shows the trajectory of a photon subject to wide-angle scattering before being returned to the receiver; in this regime the extra path length leads to the photon appearing to have originated below the cloud. The relevant regime is determined by whether such returned photons typically lie within or outside the receiver footprint.

wave radar observations of light to moderate rain.

1. Single scattering. In an optically thicker medium, provided that any scattered photons leave the field-of-view of the receiver and are not detected (except those in the exact backscatter direction), the apparent backscatter measured at a range r is given simply by

$$\hat{\beta}(r) = \beta(r) \exp[-2\delta(r)], \quad (1)$$

where $\delta(r)$ is the optical depth of clouds, aerosols and gases between the instrument and r . Such conditions are

*Corresponding author address: Department of Meteorology, Earley Gate, PO Box 243, Reading RG6 6BB, United Kingdom.
E-mail: r.j.hogan@reading.ac.uk

experienced by a ground-based lidar observing an optically thick aerosol layer, a mm-wave radar observing liquid clouds, and a cm-wave radar observing heavy rain.

2. *Quasi-small-angle multiple scattering.* In the case of lidar, where cloud particles are typically much larger than the wavelength, Babinet’s principle states that half of the extinguished energy is scattered into a narrow forward lobe of $1/e$ half-width $\Theta = \lambda/(\pi a)$, where λ is the wavelength and a is the radius of the particle (van de Hulst 1957; Hogan 2006). For typical ground-based lidar observations of ice and liquid clouds, and spaceborne lidar observations of ice clouds and aerosols, the field of view is such that these quasi-small-angle (QSA) forward-scattered photons may remain within the field-of-view of the detector and contribute to the apparent backscatter, whereas photons that experience wide-angle scattering will typically be transported outside the field-of-view such that they are not detected. As the distance traveled by photons that have only undergone QSA scattering is approximately the same as unscattered photons, the time of travel can still be converted unambiguously into the distance of the target from the instrument, even though the intensity is more difficult to interpret. The condition for this behavior to occur is

$$l_s \Theta \lesssim X \ll l_t, \quad (2)$$

where X is the width of the “footprint” projected by the field-of-view of the receiver at the range of the target, $l_s = 1/\alpha_s$ is the scattering mean-free-path, α_s is the scattering coefficient, $l_t = l_s/(1 - \tilde{\omega}g)$ is the transport mean-free-path, $\tilde{\omega}$ is the single scattering albedo and g is the asymmetry factor defined as the average cosine of the scattering phase function: $g = \langle \cos \theta \rangle$.

3. *Wide-angle multiple scattering.* When X is of the same order or larger than l_t , then wide-angle scattered photons may remain within the field-of-view and be detected, but with a time delay that makes them appear to have originated at a range beyond the distance to which they actually penetrated. This “pulse stretching” is illustrated in Fig. 1 and is particularly visible in spaceborne lidar observations of liquid water clouds (Platt and Winker 1995), but is also apparent in observations by the Cloud-Sat 94-GHz radar in deep tropical convective precipitation (Battaglia et al. 2007).

Part 1 of this two-part paper presents a very fast method for calculating QSA multiple scattering (Regime 2 above), which is suited for application on its own to ground-based lidar. Part 2 (Hogan and Battaglia 2007) then presents a method to model wide-angle multiple scattering (Regime 3 above) using the time-dependent two-stream approximation. Even in Regime 3, the apparent backscatter in the first few optical depths of penetration into the medium are dominated by scattering in Regimes 1 (for radar) or 2 (for lidar), requiring a hybrid approach. This is described fully in Part 2.

There is extensive literature on methods to model QSA multiple scattering. The simplest method was proposed by Platt (1973), who introduced a term η into (1) to obtain

$$\hat{\beta}^d(r) = \beta(r) \exp[-2\eta\delta(r)], \quad (3)$$

where the superscript “ d ” is used to distinguish between this “quasi-direct” return and the return due to wide-angle scattering in Part 2. The value of η can vary between 1 (the single-scattering limit) and $1/2$ (the wide field-of-view limit). The latter case corresponds to all the photons in the forward lobe remaining within the receiver field-of-view; thus η has the effect of reducing the effective optical depth such that these photons are treated as if they had not been scattered at all. If the medium is represented by an N -point profile of extinction values, then the calculation of (3) is $O(N)$ efficient. However, the problem with this approach is that forward-scattered photons progressively escape from the field-of-view with increasing distance downstream of the scattering event, implying that η should increase with range. Unfortunately, there is no satisfactory theory for deriving η and its range dependence for a particular lidar geometry and scattering phase function.

Eloranta (1998) took a more rigorous approach, explicitly calculating each scattering order separately. His algorithm achieved $O(N^m/m!)$ efficiency when considering up to m orders of scattering. Hogan (2006) (hereafter H06) used Eloranta’s approach for double scattering, but treated all orders of scattering above second order together in such a way that the whole algorithm was $O(N^2)$ efficient. This was achieved by modeling the variance and covariance of photon position and direction. It was found to be typically as accurate as Eloranta’s algorithm taken to 5th order, but much more efficient.

In section 2 of this paper it is shown that the H06 method can be regarded as one of a family of “photon variance-covariance” (hereafter PVC) methods, a new example of which is then presented that achieves $O(N)$ efficiency with only a small reduction in accuracy compared to H06. In section 3 the extra calculations necessary to account for anisotropic scattering in the near-180° direction by liquid water droplets and ice particles are described. This is followed by comparisons with existing methods for QSA multiple scattering in section 4. An fast approximate method to estimate the Jacobian is then presented in section 5, which is necessary if this method is to be used as the forward model in a variational retrieval scheme (e.g. Delanoë and Hogan 2007).

2. Method

a. Introductory considerations

The main scatterers that are important for lidar are cloud particles, aerosols and molecules. We denote the combined extinction coefficient of all scatterers and ab-

sorbers versus range as $\alpha(r)$. However, only cloud particles are sufficiently large compared to the wavelength to produce a narrow forward lobe in the phase function. Since in Part 1 we are only concerned with QSA multiple scattering, we introduce the ‘‘QSA extinction coefficient’’, $\alpha^q(r)$, to represent the extinction that is caused only by cloud particles. It should be noted that the optical depth in (1) is defined in terms of the total extinction: $\delta(r) = \int_0^r \alpha(r) dr$. The scattering by aerosols and molecules (and the component of scattering by cloud particles that is not in the forward lobe) can still contribute to multiple scattering, but only in the wide-angle regime addressed in Part 2. Note that for radar, even the largest precipitation particles are too small to produce a significant forward lobe, so any multiple scattering will be in the wide-angle regime.

The formulation of the algorithm is simplified by the use of the ‘‘equivalent-medium theorem’’, which has been proved to be valid under the QSA approximation (Katsev et al. 1997; Bissonnette 2005). This theorem states that the backscatter measured in a medium is the same as that from an equivalent hypothetical medium that has twice the extinction and scattering coefficients (but the same phase function) as the true medium on the outward journey, but zero extinction and scattering on the return journey. Thus the two-way problem is transformed into a simpler one-way propagation problem.

The following assumptions are made in common with Eloranta (1998) and H06: (i) both the laser divergence and the forward-scattering lobe from a distribution of particles may be represented as Gaussians, (ii) the extra path length of multiply scattered photons may be neglected, (iii) the lidar is mono-static so that the problem has azimuthal symmetry, and (iv) all angles are small such that $\sin \theta \simeq \theta$.

b. Calculation of the energy and variance of the outgoing photon distribution

Using similar nomenclature to H06, we consider a laser transmitter that emits a short pulse of total energy P_0 in a Gaussian beam with a $1/e$ angular half-width of ρ_r . At a distance r from the instrument, the energy density of outgoing unscattered photons (in J m^{-2}) in the equivalent medium is a function of r and the distance perpendicular to the laser axis, s :

$$E_u(r, s) = \frac{P_u(r)}{\pi s_u^2(r)} \exp \left[-\frac{s^2}{s_u^2(r)} \right], \quad (4)$$

where the variance of the lateral distance of the unscattered photons to the lidar axis is

$$\overline{s_u^2}(r) = \rho_r^2 r^2, \quad (5)$$

and the total unscattered energy reaching range r is $P_u(r) = P_0 \exp[-2\delta(r)]$. Note that the factor of 2 in the

exponent is due to the doubled optical depth of the equivalent medium.

The main task of the algorithm is to estimate the distribution of forward-scattered photons as a function of r and s . It is convenient to treat the forward-scattered photon distribution as the sum of several separate distributions (E_a, E_b , etc.), such that the ‘‘combined’’ distribution (unscattered plus forward scattered) is given by

$$E(r, s) = E_u(r, s) + E_a(r, s) + E_b(r, s) + \dots, \quad (6)$$

from which the apparent backscatter may be calculated (section 2d). In the case of the H06 algorithm, E_a would represent photons forward scattered only a single time (i.e. those that contribute to double scattering) while E_b would represent photons forward scattered multiple times. These distributions can be characterized by their total energies (P, P_a , etc.) and spatial variances ($\overline{s^2}, \overline{s_a^2}$, etc.), which are functions of r alone. It is convenient to normalize the energies by the energy in the unscattered beam such that $\hat{P} = P/P_u$ and similarly for \hat{P}_a etc. The normalized energies and the variances then satisfy

$$\begin{aligned} \hat{P} &= 1 + \hat{P}_a + \hat{P}_b + \dots; \\ \hat{P} \overline{s^2} &= \overline{s_u^2} + \hat{P}_a \overline{s_a^2} + \hat{P}_b \overline{s_b^2} + \dots. \end{aligned} \quad (7)$$

It turns out that the easiest way to calculate the variables describing the forward-scattered distributions is to first calculate the corresponding variables for the full distribution, $\hat{P}(r)$ and $\overline{s^2}(r)$. Note that these variables have exact definitions even though it is not implied that the full distribution has a particular form (such as Gaussian). The normalized total energy of the combined distribution is given by

$$\hat{P}(r) = \exp \left[\int_0^r \alpha^q(r') dr' \right], \quad (9)$$

which expresses the fact that forward scattering by cloud particles has the effect of reducing the effective extinction by a factor $\alpha^q/2$, leading to \hat{P} increasing with range. The use of the equivalent medium theorem leads to a doubling of the $\alpha^q/2$ factor when used in (9).

The bulk of this section is concerned with how to calculate $\overline{s^2}(r)$ exactly, subject to the assumptions given at the end of section 2a. In order to do this with $O(N)$ efficiency, it is necessary to keep track of two other variables, the variance of photon direction, $\overline{\zeta^2}(r)$, and a variable representing the covariance of photon position and direction,¹ $C^{s\zeta}(r)$. We require differential equations to express how these variables vary with range. Consider first the spatial variance, which is the sum of the variances in the two orthogonal directions: $\overline{s^2} = \overline{x^2} + \overline{y^2}$. Figure 2 shows that if a photon travels away from the lidar a short distance dr then its lateral distance in the x direction changes by

$$dx = \zeta_x dr. \quad (10)$$

¹Note that $C^{s\zeta}$ was written as $\overline{s\zeta}$ by H06, which is not strictly correct.

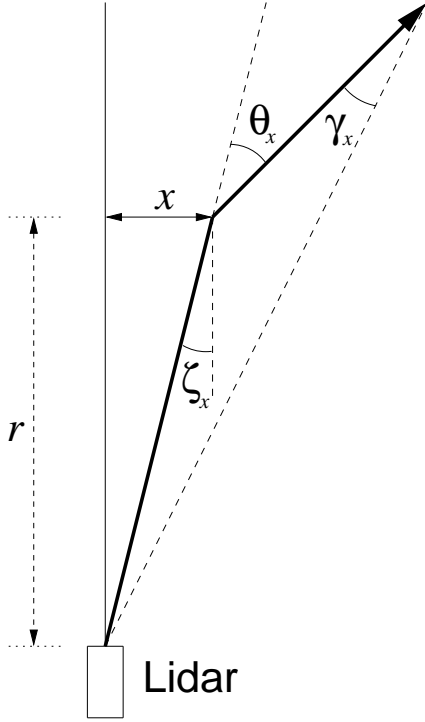


FIG. 2: Schematic of the trajectory of a single photon (thick line) in one of the two directions perpendicular to the lidar axis (thin vertical line). At range r the photon has a distance x from the lidar axis and an angle ζ_x with respect to it. It is then scattered by an angle θ_x . If it is subsequently scattered back towards the lidar, then the “scattering co-angle” is denoted by γ_x . Note that the x axis has been exaggerated with respect to the r axis in this diagram, as in practice all of these angles are small. The same diagram could be drawn in the r - y plane to define the variables y , ζ_y , θ_y and γ_y .

Hence

$$dx^2 = 2xdx = 2x\zeta_x dr. \quad (11)$$

Taking the mean over all outgoing photons yields $d\bar{x}^2 = 2x\bar{\zeta}_x dr$. By defining $C^{s\zeta} = x\bar{\zeta}_x + y\bar{\zeta}_y$, we obtain

$$d\bar{s}^2 = 2C^{s\zeta} dr. \quad (12)$$

Thus the evolution of \bar{s}^2 depends on the evolution of the covariance term $C^{s\zeta}$. To calculate $C^{s\zeta}$, we first consider the evolution of $(x\zeta_x)$. By definition

$$d(x\zeta_x) = \zeta_x dx + x d\zeta_x. \quad (13)$$

Substituting (10) into the first term on the right hand side and averaging over all photons yields $d\bar{x}\bar{\zeta}_x = \bar{\zeta}_x^2 dr$. The second term on the right hand side of (13) has disappeared in the averaging process, because $d\zeta_x$ represents the change in propagation angle due to a scattering event, which is uncorrelated to the position x . The definition $\bar{\zeta}^2 = \bar{\zeta}_x^2 + \bar{\zeta}_y^2$ then yields

$$dC^{s\zeta} = \bar{\zeta}^2 dr. \quad (14)$$

Thus the evolution of $C^{s\zeta}$ depends on the evolution of $\bar{\zeta}^2$. The propagation angle of photons within the distribution under consideration is only changed by QSA forward-scattering events, because wide-angle scattered photons are lost from the distribution. As the distribution propagates through the medium, the effect of forward-scattering is to increase the variance of photon propagation angle. H06 showed that the standard deviation of the scattering angle may be defined as $\Theta = \lambda/(\pi a_G)$, where a_G is the equivalent-area radius of the size distribution such that $\pi a_G^2 = \langle G \rangle$, and $\langle G \rangle$ is the mean cross-sectional area of the scattering particles. Thus the evolution of $\bar{\zeta}^2$ is governed by

$$d\bar{\zeta}^2 = \alpha^q \Theta^2 dr. \quad (15)$$

Note that in this equation there has been a cancellation of the factor of 2 due to the use of an equivalent medium by the factor of 1/2 due to the fact that only half of the extinguished energy ends up in the forward lobe.

In practice, the variables α^q and Θ^2 are defined at discrete points in range, so it is necessary to numerically integrate (12), (14) and (15) forward together. It is assumed that the values at range gate i , α_i^q and Θ_i^2 , are constant between the ranges $r_{i-1/2}$ and $r_{i+1/2}$. Before the photons have encountered any QSA scatterers, the three variables $\bar{\zeta}^2$, $C^{s\zeta}$ and \bar{s}^2 are the same as for the unscattered distribution and are determined by the geometry of the instrument such that $\bar{\zeta}^2 = \bar{\zeta}_u^2 = \rho_{tr}^2$, $C^{s\zeta} = C_u^{s\zeta} = r\rho_{tr}^2$ and $\bar{s}^2 = \bar{s}_u^2 = r^2\rho_{tr}^2$ (Hogan 2006). Given the values of these variables at half-gate $i - 1/2$, we may calculate them at half-gate $i + 1/2$ as follows. First we integrate (15) across the range gate to get

$$\bar{\zeta}_{i+1/2}^2 = \bar{\zeta}_{i-1/2}^2 + \alpha_i^q \Theta_i^2 \Delta r_i, \quad (16)$$

where $\Delta r_i = r_{i+1/2} - r_{i-1/2}$. Next we substitute $\bar{\zeta}^2 = \bar{\zeta}_{i-1/2}^2 + \alpha_i^q \Theta_i^2 \times (r - r_{i-1/2})$ into (14) and integrate:

$$\begin{aligned} C_{i+1/2}^{s\zeta} &= C_{i-1/2}^{s\zeta} + \int_{r_{i-1/2}}^{r_{i+1/2}} \bar{\zeta}^2 dr \\ &= C_{i-1/2}^{s\zeta} + \bar{\zeta}_{i-1/2}^2 \Delta r_i + \alpha_i^q \Theta_i^2 \Delta r_i^2 / 2. \end{aligned} \quad (17)$$

Likewise, by integration of (12) we obtain

$$\begin{aligned} \bar{s}_{i+1/2}^2 &= \bar{s}_{i-1/2}^2 + 2C_{i-1/2}^{s\zeta} \Delta r_i \\ &\quad + \bar{\zeta}_{i-1/2}^2 \Delta r_i^2 + \alpha_i^q \Theta_i^2 \Delta r_i^3 / 3. \end{aligned} \quad (18)$$

Due to modifications made to these variables in section 2c, it is necessary to define the “sequential” form of (9) as

$$\hat{P}_{i+1/2} = \hat{P}_{i-1/2} \exp(\alpha_i^q \Delta r). \quad (19)$$

Therefore, sequential application of (16)–(19) allows \hat{P} , $\bar{\zeta}^2$, $C^{s\zeta}$ and \bar{s}^2 to be calculated at each half-gate.

The strength of this method is that arbitrary orders of scattering are represented without having to model each of

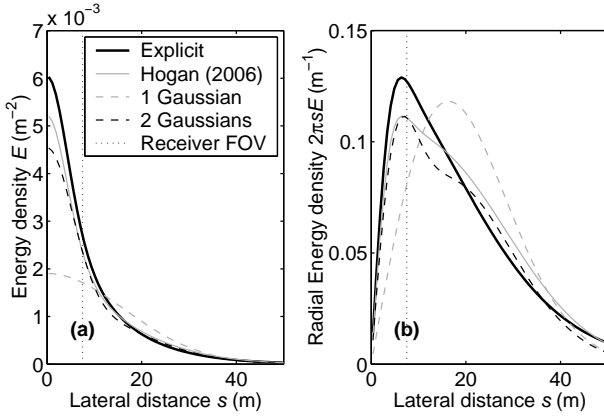


FIG. 3: (a) Lateral distribution of outgoing forward-scattered photon energy (normalized by the transmitted energy) for light that has penetrated to an (equivalent-medium) optical depth of 3 in a homogeneous medium with a forward-scattering lobe of width $\Theta = 0.015$. The initial photon distribution has a lateral standard deviation of $\rho_w r = 5$ m. (b) The same but after azimuthal integration (i.e. multiplication by $2\pi s$). The thick black line is from an explicit calculation taken to 7th-order scattering, consisting of the sum of over 8000 Gaussians, representing each of the possible combination of the ten range gates in which a photon could be forward scattered. The remaining solid and dashed lines represent the various approximations discussed in the text. The dotted line at $s = 7.5$ m indicates the receiver field-of-view half-width corresponding to a footprint full-width of $X = 15$ m.

them explicitly. The use of the differential equation (15) and its subsequent integration over a range gate in (16) even allows a photon to be scattered several times within a single range gate.

c. Estimation of the shape of the forward-scattered distribution

The previous subsection has shown how the energy and variance of the full photon distribution may be calculated exactly. The simplest strategy for estimating the contribution of multiple scattering to apparent backscatter would be to treat all forward-scattered photons as a single Gaussian of energy \hat{P}_a and spatial variance $\overline{s^2}_a$, and estimate these variables from (7) and (8) (i.e. neglecting \hat{P}_b , $\overline{s^2}_b$, etc). This approach is tested in Fig. 3, which shows the forward-scattered photon distribution calculated “explicitly” for a simple homogeneous cloud, along with several approximations. The explicit calculation considered all possible ways that a multiply scattered photon could arrive at its destination by recursive application of Eqs. 15–18 in H06, thereby producing the distribution that is implicitly represented by the Eloranta (1998) method.

Since the return journey after backscattering in the equivalent medium is in vacuum, the apparent backscatter is proportional to the area under the curve in Fig. 3b up to the vertical dotted line, which denotes the half-width of the receiver footprint, $X/2$. It can be seen that the single-Gaussian approximation (the gray dashed line) does not well match the true distribution, which is dis-

tinctly “leptokurtic”. The disagreement is especially evident for $s < X/2$, indicating that apparent backscatter would be significantly underestimated. This is despite the Gaussian having both the correct energy (i.e. the total area under the curve in Fig. 3b) and variance.

A more sophisticated representation of the photon distribution is clearly needed. The gray solid line in Fig. 3 shows the approximation employed by H06, which used an explicit treatment of double-scattering (corresponding to a Gaussian for each of the possible locations at which photons could be forward scattered) but treated all higher-order scatterings by a single Gaussian. The distribution is represented significantly better. It is now shown that almost the same performance can be achieved with only two Gaussians (E_a and E_b), thereby avoiding the nested loop required by H06.

The problem with the single-Gaussian representation is that although its variance $\overline{s^2}_a$ is calculated exactly, this variable is often dominated by the contribution of photons that have escaped from the receiver field-of-view and contribute nothing to the apparent backscatter. What is required is some way to model just those photons within the field-of-view. This is achieved by carrying out the procedure described in section 2b twice, the second time with an adjustment after each range gate to ensure that implied width of the single Gaussian E_a does not exceed the receiver footprint width at that height. If it does then each of the variables is adjusted to remove those photons that were scattered too far outside the field-of-view. So at half-gate $i + 1/2$, application of (16)–(19) yields the variables describing the full distribution \hat{P} , $\overline{s^2}$, $C^{s\zeta}$ and $\overline{\zeta^2}$. These are used to calculate the corresponding variables of the single Gaussian (\hat{P}_a , $\overline{s^2}_a$, $C^{s\zeta}_a$ and $\overline{\zeta^2}_a$) via (7) and (8) but without the “b” terms. Note that $C^{s\zeta}$ and $\overline{\zeta^2}$ are weighted averages so an analogous expression to (8) may be used. The width of the forward-scattered distribution is then tested to see if it exceeds the half-width of the receiver field-of-view, $X/2 = \rho_{fov} r$ (where r is the range to gate $i + 1/2$) and if it does then a scaling factor f is defined:

$$f = \begin{cases} (\rho_{fov} r)^2 / \overline{s^2}_a; & \overline{s^2}_a < (\rho_{fov} r)^2 \\ 1; & \overline{s^2}_a \geq (\rho_{fov} r)^2 \end{cases} \quad (20)$$

This is then used to scale the variance and total energy as follows:

$$\overline{s^2}_a \leftarrow f \overline{s^2}_a; \quad (21)$$

$$\hat{P}_a \leftarrow f \hat{P}_a, \quad (22)$$

where (22) ensures that when the variance is reduced, the peak energy (i.e. E_a at $s = 0$) is preserved. The appropriate way to scale $\overline{\zeta^2}_a$ and $C^{s\zeta}$ is less obvious, since these variables depend on the joint distribution of the four variables x , y , ζ_x and ζ_y , and in particular the x - ζ_x and y - ζ_y correlations (no other correlations exist). Using a method

of Monte Carlo sampling from two bi-variate Normal distributions, it has been found that the appropriate scalings are

$$C_a^{s\zeta} \leftarrow fC_a^{s\zeta}, \quad (23)$$

$$\overline{\zeta}_a^2 \leftarrow (f\rho^2 + 1 - \rho^2)\overline{\zeta}_a^2, \quad (24)$$

where the correlation coefficient between position and direction is given by $\rho = C_a^{s\zeta}(\overline{s}_a^2\overline{\zeta}_a^2)^{-1/2}$. Equation 24 has logical limits: in the case that position and direction are uncorrelated ($\rho = 0$), sampling photons by their position has no effect on the variance of their direction so $\overline{\zeta}_a^2$ is unchanged. Conversely, if they are perfectly correlated then sampling photons by position has the same fractional effect on $\overline{\zeta}_a^2$ as it does on \overline{s}_a^2 .

After these scalings have been performed at half-gate $i + 1/2$, the variables describing the unscattered distribution are added back on using (7) and (8), and the procedure in section 2b is repeated to obtain the variables of the full distribution at half-gate $i + 3/2$, and so on. Thus we obtain a profile of \hat{P}_a and \overline{s}_a^2 describing a single Gaussian whose width is constrained by the receiver field-of-view. The photons removed from the distribution may still contribute to the backscatter by being forward-scattered back into the receiver field-of-view. Their energy and width (\hat{P}_b and \overline{s}_b^2) may be calculated from (7) and (8) using the *original* calculation of \hat{P} and \overline{s}^2 , i.e. without the scaling expressed in Eqs. 21–24. Thus we have two Gaussians with which to represent the forward-scattered photon distribution. This is represented by the black dashed line in Fig. 3 and can be seen to be very similar to the H06 distribution up to the receiver half-width. However, the calculations described in this section are $O(N)$ efficient rather than the $O(N^2)$ required by the H06 method.

It should be stressed that other methods are possible within the PVC framework. For example, if higher accuracy were required than shown by the approximations in Fig. 3, and $O(N^3)$ efficiency could be tolerated, then a promising approach might be to use an explicit method of Eloranta (1998) for double and triple scattering, but to represent all higher-order scatterings by a single Gaussian using the PVC approach.

d. Calculation of apparent backscatter

The apparent backscatter $\hat{\beta}^d$ can be expressed as the sum of the contributions from single and multiple scattering

$$\hat{\beta}^d = \hat{\beta}_1 + \hat{\beta}_a + \hat{\beta}_b + \dots, \quad (25)$$

where $\hat{\beta}_1 = \beta \exp(-2\delta)$ is the attenuated backscatter due to single scattering (expressed in terms of true backscatter coefficient β and the optical depth to the point of observation δ), and the remaining terms correspond to the distributions used to describe the forward-scattered photons in section 2. To determine $\hat{\beta}_a$ we need to know the fraction of photons in distribution E_a that are detected by the

receiver. In the equivalent medium, the return journey of any backscattered photons is in vacuum, so the only photons that can be detected by a telescope with a half-angle field-of-view of ρ_{fov} are those with a lateral distance of $s < \rho_{\text{fov}}r$ (corresponding to the area under the curve to the left of the dotted line in Fig. 3b). Thus we have

$$\hat{\beta}_a = \hat{\beta}_1 F(r) \frac{\int_0^{\rho_{\text{fov}}r} E_a(r, s) s ds}{\int_0^{\rho_{\text{fov}}r} E_u(r, s) s ds}, \quad (26)$$

and similarly for $\hat{\beta}_b$. In (26), the ‘‘anisotropic backscatter factor’’ F can be used to account for an anisotropic phase function near 180° , as described in section 3. However if the phase function is close to isotropic near 180° then we simply use $F = 1$.

Substitution of the appropriate Gaussian distributions (of the form in Eq. 4) for both E_u and E_a yields

$$\hat{\beta}_a(r) = \hat{\beta}_1(r) F(r) \hat{P}_a(r) \frac{1 - \exp(-\rho_{\text{fov}}^2 r^2 / \overline{s}_a^2)}{1 - \exp(-\rho_{\text{fov}}^2 / \rho_{\text{tr}}^2)}, \quad (27)$$

and similarly for $\hat{\beta}_b$. In some cases the lidar receiver operates in the diffraction limit, in which case the receiver pattern would be better described as a Gaussian of $1/e$ half-width ρ_{fov} , rather than as a ‘‘top-hat’’ function used above. In this case one should use:

$$\hat{\beta}_a(r) = \hat{\beta}_1(r) F(r) \hat{P}_a(r) \frac{1 + \rho_{\text{tr}}^2 / \rho_{\text{fov}}^2}{1 + \overline{s}_a^2 / \rho_{\text{fov}}^2 r^2}. \quad (28)$$

See Part 2 for further details.

In practice, the extinction and true backscatter coefficients will be input on a discrete grid, and care must be taken to ensure that the calculated apparent backscatter is the mean for each layer. This is particularly true if the optical depth of any individual layer is of order or greater than unity because then substantial attenuation occurs within a single layer. We also need to deal with the problem that \hat{P} and \overline{s}^2 are calculated on a different grid to extinction and true backscatter. The numerical details of how this is overcome are presented in the appendix.

3. Accounting for anisotropic phase functions near 180°

For singly scattered photons to be detected, they must be scattered through exactly π radians, so the backscatter coefficient is sufficient to determine the intensity of the return echo. For QSA multiple scattering, small-angle forward-scattering events on the outward or return journeys mean that photons scattered in the backward direction by an angle less than π may also be detected by the receiver. Hence we need to consider the shape of the phase function in the backward direction, and the distribution of near- π scattering angles that can result in a photon being detected. This enables the term F in (26) to be estimated.

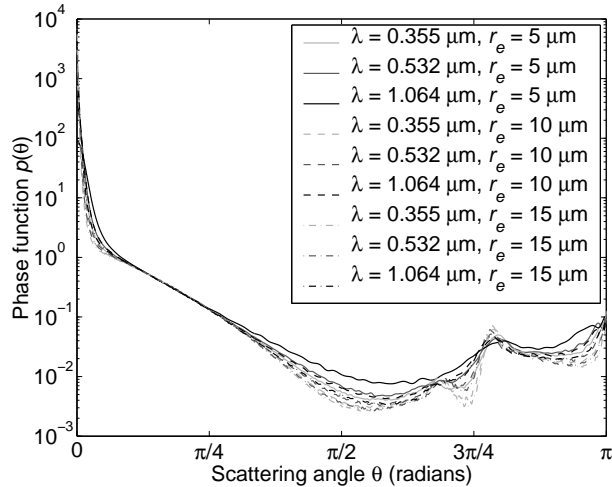


FIG. 4: The scattering phase function of a gamma distribution (of shape parameter 2) of water droplets for three commonly used lidar wavelengths and three values of effective radius (r_e) typical of liquid water clouds. The calculations were performed using Mie theory.

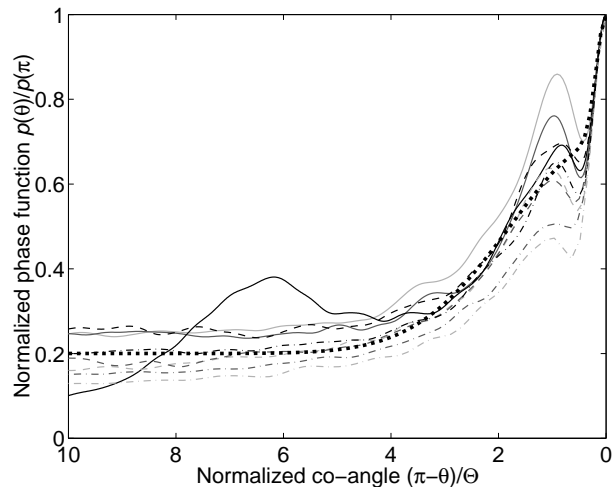


FIG. 5: Droplet scattering phase function in the vicinity of the backward direction, normalized by the backscatter value $p(\pi)$, versus the scattering co-angle normalized by Θ (defined in the text). The thin lines correspond to the same wavelengths and effective radii as in Fig. 4, while the large dots correspond to the double-Gaussian fit discussed in section 3a and represented by (29).

a. Parameterizing the phase function near 180°

We first consider the scattering by distributions of liquid water droplets. Figure 4 shows the scattering phase function for three common lidar wavelengths and the range of effective radius typically found in stratocumulus (Miles et al. 2000). The phase function can be seen to exhibit a peak in scattering for scattering angles θ close to π , while at smaller angles the scattering decreases before reaching a secondary peak corresponding to the “halo” phenomenon. We seek to parameterize the phase function near $\theta = \pi$. Following van de Hulst (1957), the “scatter-

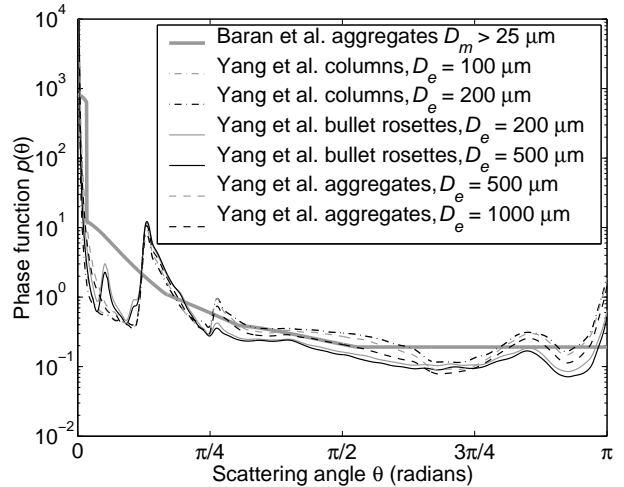


FIG. 6: The scattering phase function at $0.55 \mu\text{m}$ for distributions of ice particles of different habits. The thick grey line corresponds to individual aggregates from Baran et al. (2001); above a maximum dimension (D_m) of $25 \mu\text{m}$ there is no dependence on size so distributions of such particles would have the same phase function. The remaining lines are from Yang et al. (2000) for gamma distributions of shape parameter 2, with various values of effective diameter (D_e).

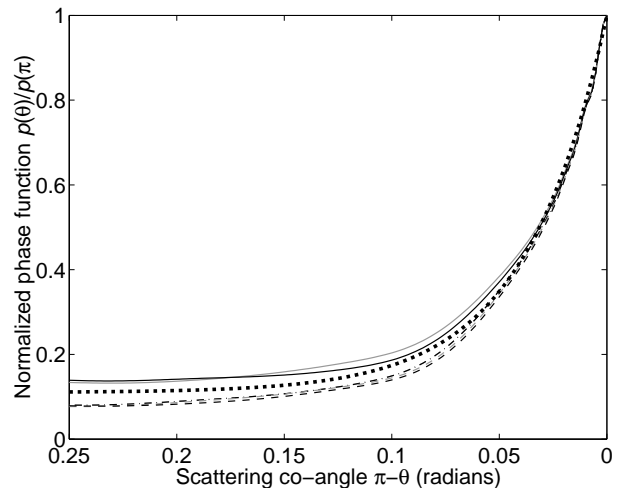


FIG. 7: The Yang et al. (2000) phase functions shown in Fig. 6, but after normalizing by the backscatter value $p(\pi)$ (thin lines). The large dots correspond to the inverse-exponential fit discussed in section 3a and represented by (30).

ing co-angle” is defined as $\gamma = \pi - \theta$. Figure 5b shows the phase function $p(\theta)$ near $\theta = \pi$, normalized by the value at $\theta = \pi$. Note that backscatter coefficient in units of $\text{m}^{-1} \text{sr}^{-1}$ is defined as $\beta = p(\pi)/4\pi$. The abscissa has also been normalized, using the variable Θ discussed in section 2b. It can be seen that the halo always peaks at $\gamma \simeq \Theta$.

The exact shape of the halo depends on the width of the droplet size distribution, which we would not expect to be able to retrieve remotely, so instead we parameterize

the shape of the phase function as the sum of a constant and two Gaussians:

$$p(\pi - \gamma)/p(\pi) = U_0 + U_1 \exp[-(V_1\gamma/\Theta)^2] + U_2 \exp[-(V_2\gamma/\Theta)^2], \quad (29)$$

where $U_0 = 0.2$, $U_1 = 0.3$, $U_2 = 0.5$, $V_1 = 4.0$ and $V_2 = 0.4$. This is represented in Fig. 5 as the thick dashed line. It can be seen to fit the actual normalized phase functions to within around 30%.

In the case of ice particles, there is some disagreement in the literature regarding the nature of the phase function, with observations tending to show much more featureless and flat phase functions than scattering calculations based on idealized ice particle shapes. This is illustrated in Fig. 6: the thin lines show calculations by Yang et al. (2000) for three different shapes over a range of sizes, while the thick line shows the smooth phase function fitted to observations by Baran et al. (2001). This discrepancy is likely to be due to the fact that most ice clouds are dominated by irregular aggregates, possibly compounded by factors such as roughened surfaces, aerosol inclusions and distortions between parallel faces (Baran 2004).

Of principal relevance to this paper is the nature of the phase function near $\theta = \pi$. Here the Baran et al. (2001) phase function is isotropic, which can be explained by the irregular particles lacking the azimuthal symmetry necessary for constructive interference, which is the cause of the peak in the phase function for spheres. By contrast, the Yang et al. (2000) phase functions all exhibit an upturn within 5° of backscatter. Figure 7 shows that when normalized by the value at backscatter, all the Yang et al. (2000) phase functions collapse on to approximately the same curve, which is well fitted by the following expression:

$$p(\pi - \gamma)/p(\pi) = (1 - W) + W \exp(-\gamma/\gamma_0), \quad (30)$$

where $W = 0.89$ and $\gamma_0 = 0.038$. Unlike the near- π peak for liquid droplets shown in Fig. 5 and indeed the forward lobe for both liquid and ice particles, the peak in the ice phase function apparently shows little dependence on particle size or wavelength (via Θ). Its cause is therefore difficult to determine.

b. Calculation of the distribution of photon co-angles that contribute to the returned power

Using an approach similar to section 2b, we now calculate the variance of the distribution of the photon scattering co-angles, weighted by their contribution to the returned power. When coupled to knowledge of the phase function near $\theta = \pi$, such as the parameterization of (29), the F term in (26) may be calculated. Note that as we are considering the equivalent medium, we need only consider forward scattering events on the outward journey;

then from the position and propagation angle, the scattering co-angle that results in a photon returning to the receiver can be determined.

Consider first the component of γ in the x -direction, γ_x . From Fig. 2 it can be seen that for a single photon $\gamma_x = \zeta_x - x/r$. Taking the square of both sides and averaging over a distribution of photons yields

$$\overline{\gamma_x^2} = \overline{(\zeta_x - x/r)^2} = \overline{\zeta_x^2} + \overline{x^2}/r^2 - 2x\overline{\zeta_x}/r. \quad (31)$$

Noting that the two components of co-angle are related by $\overline{\gamma^2} = \overline{\gamma_x^2} = \overline{\gamma_y^2}$, and similarly for the other quantities, we obtain

$$\overline{\gamma^2} = \overline{\zeta^2} + \overline{s^2}/r^2 - 2C^{s\zeta}/r. \quad (32)$$

This operation may be applied to any distribution of photons (e.g. E or E_a in Eq. 6) to obtain the corresponding variance of the co-angle. In practice it is sufficiently accurate and numerically convenient to calculate $\overline{\gamma^2}$ for the combined distribution $E_a + E_b$, thereby producing one value of F that may be applied in (27) to obtain both $\hat{\beta}_a$ and $\hat{\beta}_b$. Likewise, this value may be applied in other PVC algorithms, e.g. H06.

The variance expressed by (32) includes all photons that have experienced QSA forward scattering and are returned to the instrument, even if their returning angle is outside the receiver field-of-view. To select photons within the field-of-view an exactly analogous procedure to (24) is applied: if $\overline{s^2} > \rho_{\text{fov}}^2 r^2$ then the following scaling is performed:

$$\overline{\gamma^2} \leftarrow \left(\rho^2 \frac{\rho_{\text{fov}}^2 r^2}{\overline{s^2}} + 1 - \rho^2 \right) \overline{\gamma^2}, \quad (33)$$

where this time ρ is the correlation coefficient between position and scattering co-angle: $\rho = C^{s\gamma}(\overline{s^2} \overline{\gamma^2})^{-1/2}$, where the term representing the corresponding covariance is derived in a similar way to (31) and is given by $C^{s\gamma} = C^{s\zeta} - \overline{s^2}/r$.

c. Calculation of anisotropic backscatter factor

The final step in this section is to calculate the backscatter correction factor F . If the normalized phase function in the near- π direction is written as $p(\pi - \gamma)/p(\pi)$ and the distribution of scattering co-angles is described by $G(\gamma)$ then we have a convolution

$$F = 2\pi \int_0^\infty \frac{p(\pi - \gamma)}{p(\pi)} G(\gamma) \gamma d\gamma. \quad (34)$$

It is assumed that the distribution of scattering co-angles is described by a Gaussian of the form

$$G(\gamma) = \frac{1}{\pi\overline{\gamma^2}} \exp\left(-\frac{\gamma^2}{\overline{\gamma^2}}\right), \quad (35)$$

and the phase function for liquid water droplets may be approximated by (29), so that integration of the resulting

expression yields

$$F = U_0 + \frac{U_1}{1 + \bar{\gamma}^2 V_1^2 / \Theta^2} + \frac{U_2}{1 + \bar{\gamma}^2 V_2^2 / \Theta^2}. \quad (36)$$

This may be substituted into (27). See the appendix for how to cope with the fact that $\bar{\gamma}^2$ is calculated at half-gates while Θ is available at full gates.

An additional consideration is the contribution from molecular scattering, the phase function of which is isotropic in the backward direction (i.e. $F = 1$). This is incorporated by making F the average of the molecular and particulate contributions, weighted by their respective backscatter coefficients.

In the case of irregular ice particles, the isotropic phase function near $\theta = \pi$ predicted by Baran (2004) implies simply $F = 1$. To apply the Yang et al. (2000) phase functions we integrate (34) over (30) to yield

$$F_a = (1 - W) + W [1 - g\pi^{1/2} \exp(g^2) \text{erfc}(g)], \quad (37)$$

where $g = (\bar{\gamma}^2)^{1/2} / 2\gamma_0$ and $\text{erfc}(\cdot)$ denotes the complementary error function. It is important to note that even with the Yang et al. (2000) phase functions, F is close to 1 for most ice clouds. This is because the equivalent-area radius for most ice clouds exceeds $50 \mu\text{m}$, corresponding to a forward-lobe width Θ of typically less than 0.003 radians. After several forward scattering events, the width of the co-angle distribution is at most a few times larger than Θ . In Fig. 7 it can be seen that for such small co-angles, the phase function is only slightly reduced from its backscatter value.

4. Testing of the algorithm

a. Comparison against other methods

To evaluate the performance of the method, we compare against the method of Eloranta (1998), taken to 7th-order scattering. A test case is constructed consisting of a liquid cloud from 1 to 1.5 km, with $\alpha = 3 \text{ km}^{-1}$ and $a_G = 10 \mu\text{m}$, and an ice cloud from 3.5 to 6 km with $\alpha = 0.6 \text{ km}^{-1}$ and $a_G = 50 \mu\text{m}$; hence both clouds have an optical depth of 1.5. Here, a_G is the equivalent-area radius, defined as the radius of a sphere that has the same cross-sectional area as the mean cross-sectional area of the actual size distribution. This scene is observed by a spaceborne 532-nm lidar at an altitude of 700 km. Molecular scattering is assumed to follow an inverse-exponential profile with scale height 8 km and a surface backscatter coefficient of $1.6 \times 10^{-6} \text{ m}^{-1} \text{ sr}^{-1}$. All calculations are performed with a vertical resolution of 50 m.

The strength of the multiple scattering depends strongly on the width of the lidar telescope footprint X on the cloud, which varies by several orders of magnitude between ground-based and spaceborne instruments.

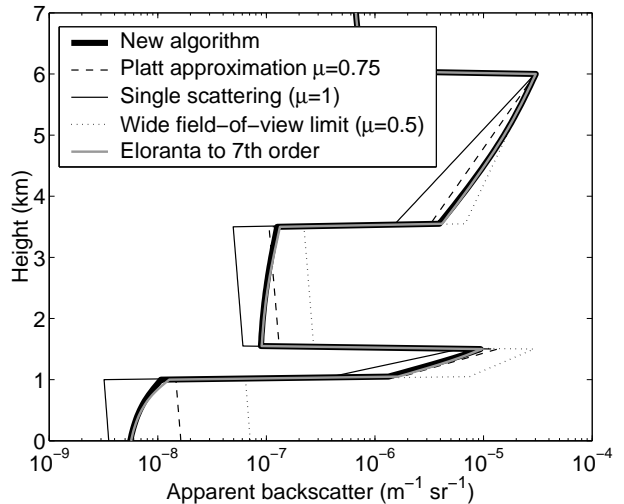


FIG. 8: Comparison of the calculated apparent backscatter for the scenario described in section 4 for a footprint at cloud top of $X = 10 \text{ m}$.

To fully explore the accuracy of the new method, it has been compared with the Eloranta (1998) model for a wide range of values. The footprint is related to the telescope half-angle ρ_{fov} by $X = 2r\rho_{\text{fov}}$. In each case the laser half-angle beam divergence has been set to $\rho_{\text{lr}} = (2/3)\rho_{\text{fov}}$. Figure 8 shows the results for a footprint of 10 m. The new algorithm agrees with Eloranta’s model to within 5% in the ice cloud and to within 10% in the liquid cloud and below, despite being much more efficient.

For comparison, the simpler method of Platt (1973) is shown for an appropriate value of μ and the performance is much poorer; in particular, this method is unable to represent the fact that close to the top of the cloud the photons largely stay within the field of view of the receiver, but further down in the profile they progressively escape, particularly in the cloud-free areas. It should be noted that both the new algorithm and the method of Platt (1973) are $O(N)$ efficient. The other lines in Fig. 8 show the two limits within which QSA calculations must fall: the single-scattering limit equivalent to $\mu = 1$, and the wide field-of-view limit equivalent to $\mu = 0.5$.

To illustrate the behavior over a full range of lidar footprints, Fig. 9 shows the percentage error in the new algorithm with respect to the Eloranta (1998) model taken to 7th order (treated as “truth”). It can be seen that the main error is in the liquid cloud for footprints less than 10 m. This is associated with a tendency to slightly underestimate the peak in the spatial distribution of forward-scattered photon shown in Fig. 3. For footprints more typical of spaceborne lidars (e.g. 90 m for Calipso and several hundred meters for LITE), the error is much reduced, implying that this algorithm is well suited to spaceborne lidar.

Figure 10 evaluates the H06 model. The performance a little better than the new algorithm in all conditions, pre-

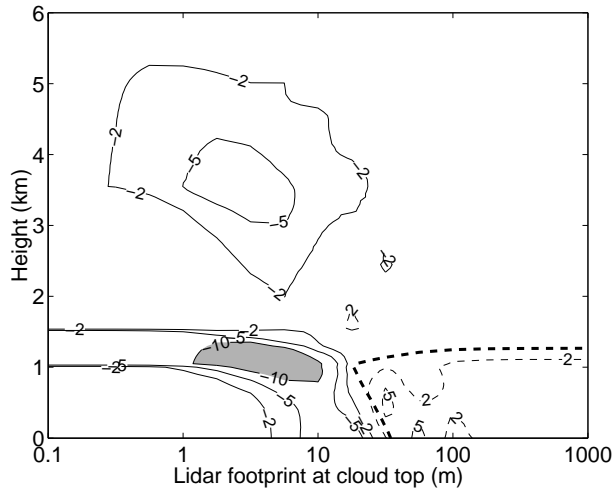


FIG. 9: Percentage difference in apparent backscatter between the new algorithm and the Eloranta (1998) algorithm taken to 7th-order scattering, as a function of height and footprint width X . The dashed lines indicate positive values, and absolute errors greater than 10% are shaded in gray. The thick dashed line in the bottom-right of the image indicate where there is greater than a 5% difference between the 6th and 7th orders of scattering of the Eloranta (1998) model, highlighting that here the Eloranta (1998) model has not fully converged.

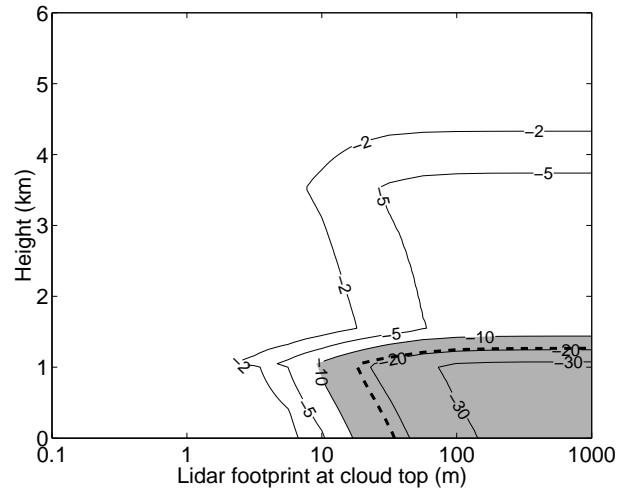


FIG. 11: As Fig. 9 but for the Eloranta (1998) model truncated at 4th order scattering.

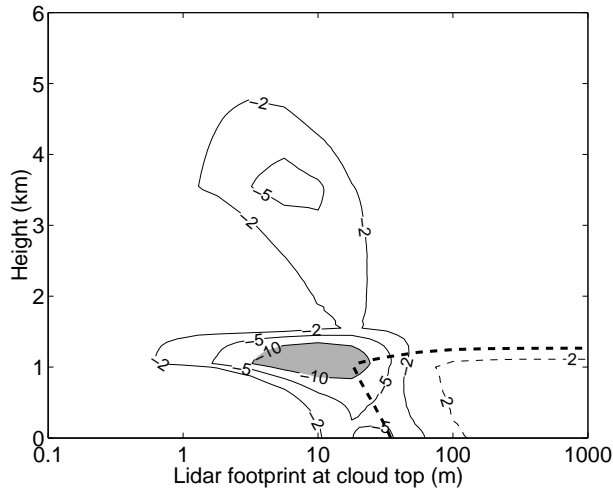


FIG. 10: As Fig. 9 but for the H06 model.

sumably due to the fact that double scattering is calculated more accurately. Figure 11 shows how Eloranta's model performs when truncated at 4th-order scattering, typically the highest order that could realistically be incorporated into a retrieval algorithm. It can be seen that substantial errors occur for optically thick liquid water cloud when observed using a footprint typical of a spaceborne lidar.

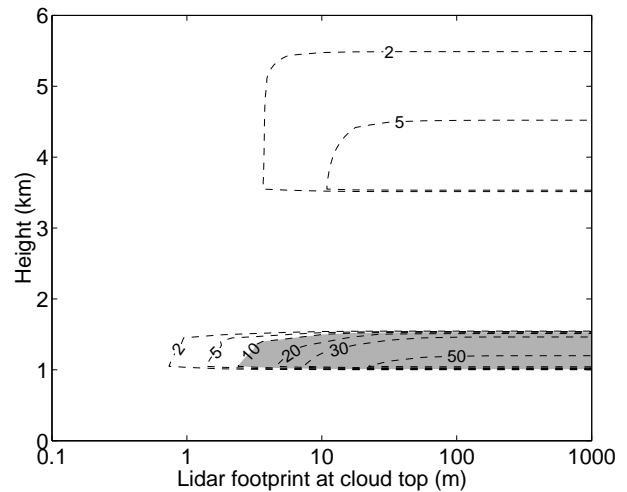


FIG. 12: Percentage error associated with neglecting the shape of the phase function in the near- 180° direction for the case shown in Fig. 9. This was calculated assuming the parameterization of the Yang et al. (2000) phase functions shown in Fig. 7 for the ice cloud, and the parameterization of the Mie phase functions shown in Fig. 5 for the liquid cloud.

b. The role of the near- 180° phase function and wide-angle scattering

It is useful to know under what conditions it is satisfactory to apply the simple QSA algorithm, and when it is necessary to include the effects of anisotropic phase functions in the backward direction and wide-angle scattering. To determine the effect of the shape of the near- 180° phase function, calculations have been performed for the case shown in Fig. 9 using the new algorithm, adopting the Mie parameterization in the liquid layer (Eqs. 29 and 36) and the parameterization of the Yang et al. (2000) phase functions (Eqs. 30 and 37) in the ice layer. Fig-

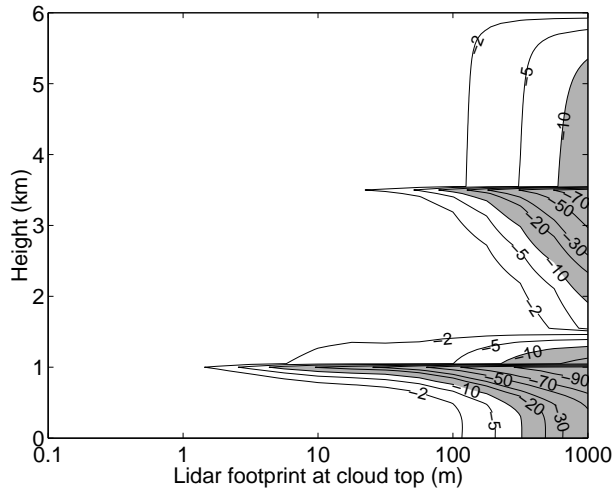


FIG. 13: Percentage error in apparent backscatter between a QSA-only model and a model that includes both QSA and wide-angle scattering, for the case shown in Fig. 9. This was calculated using the new model for QSA scattering and the time-dependent two-stream approximation described in Part 2 for wide-angle scattering. The liquid clouds was assumed to have an asymmetry factor of 0.85 while the ice cloud was assigned a value of 0.7. Both had a single-scattering albedo of unity.

ure 12 shows the results in terms of the error associated with not representing this effect. The difference in the ice cloud is at most around 7%, while in the liquid cloud it exceeds 50% for receiver footprints greater than around 20 m. There is no difference in the molecular scattering regions since the shape of the phase function in the backward direction does not affect the way that photons are forward-scattered as they propagate. There are two reasons why one should usually expect smaller differences in ice clouds than shown in this case. First, the assumed particle radius of $50 \mu\text{m}$ is at the lower end of what is typical of cirrus clouds, and larger particles lead to a narrower forward lobe and hence a smaller scattering co-angle and an effective backscatter coefficient more similar to the actual value. Second, as discussed in section 3a, the Yang et al. (2000) phase functions may not be particularly representative of most ice clouds in nature, which have a flatter phase function in the backward direction (Baran 2004).

Figure 13 depicts the error resulting from neglecting the contribution from wide-angle scattering. For footprints less than 100 m the only significant error is in the molecular region just beneath cloud base, where pulse stretching of several hundred meters enhances the return. The lack of any significant error within the ice clouds for footprints less than 100 m indicates that ice-cloud retrieval algorithms (e.g. Donovan et al. 2001; Delanoë and Hogan 2007) will be accurate from space with a simple QSA-only multiple-scattering model that also assumes an isotropic phase function in the backward direction. Nonetheless, if the molecular scattering below the cloud is to be used as an optical depth constraint then care should

be taken immediately below cloud where wide-angle scattering is important.

In the case of liquid clouds observed from space, there is a need to include both anisotropic phase functions and wide-angle scattering if the return is to be modeled accurately. It should be stressed that with an optical depth of 1.5, the liquid cloud in this example is less optically thick than most such clouds in reality, for which the error associated with using a QSA-only model will be much larger. The greater dominance of wide-angle scattering for footprints of several hundred meters is in agreement with the large amount of multiple scattering observed by the LITE lidar (Platt and Winker 1995).

5. Calculation of the Jacobian

In variational retrieval schemes (e.g. Delanoë and Hogan 2007), not only must the forward model provide the apparent backscatter at each gate, it should also provide the Jacobian matrix, consisting of the partial derivatives of apparent backscatter at each gate with respect to the input “state variables” such as extinction coefficient at every gate, i.e. $\partial \hat{\beta}_j^d / \partial \alpha_i$. To fill the elements of an $N \times N$ matrix is clearly at least an $O(N^2)$ process, so this must be done as efficiently as possible if the calculation of the Jacobian is to be commensurate in speed with the $O(N)$ efficiency of the main algorithm. An approximate Jacobian may be calculated by making use of the Platt (1973) expression (Eq. 3). First we rewrite (3) in a simple discrete form and in terms of the natural logarithm of backscatter:

$$\ln \hat{\beta}_j^d = \ln \beta_j - 2\eta_j \delta_{j-1/2} \quad (38)$$

$$= \ln \beta_j - 2\eta_j \sum_{i=1}^{j-1} \alpha_i \Delta r_i. \quad (39)$$

Equation 38 is used to calculate η at each gate as a function of variables calculated within the algorithm: $\eta_j = \ln(\beta_j / \hat{\beta}_j^d) / (2\delta_{j-1/2})$. Making the approximation that $\partial \eta_j / \partial \alpha_i = 0$, the Jacobian can be calculated from (39) to obtain

$$\frac{\partial \ln \hat{\beta}_j^d}{\partial \alpha_i} = -2\eta_j \Delta r_i \quad (40)$$

for $i < j$, and $\partial \ln \hat{\beta}_j^d / \partial \alpha_i = 0$ otherwise.

6. Conclusions

This paper has presented a fast model for calculating the multiply scattered lidar returns from clouds in the quasi-small-angle regime. It is shown to be one of a family of possible methods based on the “photon variance-covariance” (PVC) modeling approach, which includes the method of Hogan (2006). It is applicable to ice-cloud observations by both ground-based and satellite lidar provided that the receiver footprint is less than around 100 m. For larger footprints or for observations of liquid clouds

it should be supplemented by the wide-angle scattering model presented in Part 2. Benchmark calculations have been performed and the execution time is found to be of the order 10^{-4} s for a profile composed of $N = 100$ points², with the execution time being proportional to N . It is therefore suitable for direct application as the “forward model” in combined radar-lidar observations of ice clouds from space (e.g. Donovan et al. 2001; Delanoë and Hogan 2007), where execution time is critical due to the high rate at which data are being recorded.

A difficulty in the past has been how to rigorously account for anisotropic phase functions in the near- 180° direction. Here it has been shown that by parameterizing the phase function of droplets and idealized ice particles near 180° , and by careful modeling of the variance of the scattering “co-angle” in large-angle scattering events, this effect can be accounted for. In liquid clouds it is found to reduce the apparent backscatter by up to 50%. In ice clouds composed of pristine crystals the effect is much less, but in any case observations suggest that most cirrus clouds are dominated by irregular particles for which the phase function is nearly isotropic in the vicinity of 180° (Baran 2004).

Acknowledgements. I am grateful to Ulla Wandinger and Anthony Baran for useful discussions on the nature of ice particle phase functions, and to Alessandro Battaglia for valuable comments on the original manuscript.

APPENDIX

Numerical implementation

In sections 2d and 3c the problem of the variables not being on the same grid was highlighted. Specifically, the input properties of the cloud such as Θ and the unattenuated backscatter β are available on one grid, while s^2 and γ^2 are calculated at the mid-points of this grid, making it difficult to apply (27) and (29). For the most accurate estimate of apparent backscatter, especially on coarse grids when significant attenuation occurs within one range gate, we define $\hat{\beta}_i^d$ as the mean apparent backscatter between ranges $r_{i-1/2}$ and $r_{i+1/2}$ (over which the extinction coefficient α_i and true backscatter coefficient β_i are constant) as follows:

$$\hat{\beta}_i^d = \frac{1}{\Delta r_i} \int_{r_{i-1/2}}^{r_{i+1/2}} \hat{\beta}^d(r) dr, \quad (41)$$

where $\Delta r = r_{i+1/2} - r_{i-1/2}$. It is convenient to define a “multiple scattering factor” as

$$M = 1 + F \times (\hat{\beta}_a + \hat{\beta}_b) / \hat{\beta}_1, \quad (42)$$

such that (25) becomes simply $\hat{\beta}^d = M\hat{\beta}_1$. To determine $\hat{\beta}_i^d$ we first calculate the multiple scattering factor at the

²Benchmark carried out on a 1-GHz Pentium 3; see Part 2 for further details.

neighboring half-gates ($M_{i-1/2}$ and $M_{i+1/2}$), since it is only dependent itself on variables at half gates. The exception is Θ in (36) which is taken at gate i for calculating F at both half-gates.

High-resolution runs of the algorithm have revealed that in most cases it is a reasonable assumption to assume that M varies exponentially between two half-gates, i.e. $M(r) = M_{i-1/2}^{1-r'} M_{i+1/2}^{r'}$, where $r' = (r - r_{i-1/2}) / \Delta r_i$ is the normalized distance between half gates $i - 1/2$ and $i + 1/2$. Noting that we may also write $\hat{\beta}_1(r') = \beta_i \exp[-2(\delta_{i-1/2} + \alpha_i \Delta r_i r')]$, (41) becomes

$$\hat{\beta}_i^d = \frac{\beta_i \exp(-2\delta_{i-1/2})}{\Delta r_i} \times \int_0^1 \exp\left[\left(\ln \frac{M_{i+1/2}}{M_{i-1/2}} - 2\alpha_i \Delta r_i\right) r'\right] dr', \quad (43)$$

which has the solution

$$\hat{\beta}_i^d = \beta_i \exp(-2\delta_{i-1/2}) \frac{M_{i-1/2} - M_{i+1/2} \exp(-2\alpha_i \Delta r_i)}{2\alpha_i \Delta r_i - \ln(M_{i+1/2}/M_{i-1/2})}. \quad (44)$$

This is straightforward to calculate at each gate.

REFERENCES

- Ackerman, T. P., and G. M. Stokes, 2003: The Atmospheric Radiation Measurement Program. *Phys. Today*, **56**, 38–44.
- Baran, A. J., 2004: On the scattering and absorption properties of cirrus cloud. *J. Quant. Spectroscopy Rad. Transfer*, **89**, 17–36.
- Baran, A. J., P. N. Francis, L.-C. Labonnote and M. Doutriaux-Boucher, 2001: A scattering phase function for ice clouds: Tests of applicability using aircraft and satellite multi-angle multi-wavelength radiance measurements of cirrus. *Quart. J. Roy. Meteorol. Soc.*, **127**, 2395–2416.
- Battaglia, A., M. O. Ajewole and C. Simmer, 2007: Evaluation of radar multiple scattering effects in CloudSat configuration. *Atmos. Chem. Phys.*, **7**, 1719–1730.
- Bissonnette, L. R., 2005: *Lidar and multiple scattering*. In *Lidar range-resolved optical remote sensing of the atmosphere*, C. Weitkamp, Ed., Springer.
- Delanoë, J., and R. J. Hogan, 2007: A variational method for retrieving ice cloud properties from combined radar, lidar and infrared radiometer. *Submitted to J. Geophys. Res.*
- Donovan, D. P., A. C. A. P. van Lammeren, H. W. J. Russchenberg, A. Apituley, R. J. Hogan, P. N. Francis, J. Testud, J. Pelon, M. Quante and J. W. F. Goddard, 2001: Cloud effective particle size and water content profile retrievals using combined lidar and radar observations - 2. Comparison

- with IR radiometer and in situ measurements of ice clouds. *J. Geophys. Res.*, **106**, 27 449–27 464.
- Eloranta, E. W., 1998: A practical model for the calculation of multiply scattered lidar returns. *Appl. Optics*, **37**, 2464–2472.
- Hogan, R. J., 2006: Fast approximate calculation of multiply scattered lidar returns. *Appl. Optics*, **45**, 5984–5992.
- Hogan, R. J., and A. Battaglia, 2007: Fast lidar and radar multiple-scattering models - 2. Wide-angle scattering using the time-dependent two-stream approximation. *Submitted to J. Atmos. Sci.*
- Hogan, R. J., D. P. Donovan, C. Tinel, M. A. Brooks, A. J. Illingworth and J. P. V. Poiares Baptista, 2006: Independent evaluation of the ability of spaceborne radar and lidar to retrieve the microphysical and radiative properties of ice clouds. *J. Atmos. Oceanic Technol.*, **23**, 211–227.
- Illingworth, A. J., R. J. Hogan, E. J. O'Connor, D. Bouniol, M. E. Brooks, J. Delanoë, D. P. Donovan, J. D. Eastment, N. Gaussiat, J. W. F. Goddard, M. Haeffelin, H. Klein Baltink, O. A. Krasnov, J. Pelon, J.-M. Piriou, A. Protat, H. W. J. Russchenberg, A. Seifert, A. M. Tompkins, G.-J. van Zadelhoff, F. Vinit, U. Willén, D. R. Wilson and C. L. Wrench, 2007: Cloudnet – Continuous evaluation of cloud profiles in seven operational models using ground-based observations. *Bull. Am. Meteorol. Soc.*, **88**, 883–898.
- Katsev, I. L., E. P. Zege, A. S. Prikhach and I. N. Polonsky, 1997: Efficient technique to determine backscattered light power for various atmospheric and oceanic sounding and imaging systems. *J. Opt. Soc. Am. A*, **14**, 1338–1346.
- Miles, N. L., J. Verlinde and E. E. Clothiaux, 2000: Cloud droplet size distributions in low-level stratiform clouds. *J. Atmos. Sci.*, **57**, 295–311.
- Nicolas, F., L. R. Bissonnette and P. H. Flamant, 1997: Lidar effective multiple-scattering coefficients in cirrus clouds. *Appl. Optics*, **36**, 3458–3468.
- Platt, C. M. R., 1973: Lidar and radiometric observations of cirrus clouds. *J. Atmos. Sci.*, **30**, 1191–1204.
- Platt, C. M. R., and D. M. Winker, 1995: Multiple scattering effects in clouds observed from LITE. In *Optics in Atmospheric Propagation and Adaptive Systems*, Anton Kohnle, Ed. *Proc. SPIE*, **2580**, 60–71.
- Stephens, G. L., D. G. Vane, R. J. Boain, G. G. Mace, K. Sassen, Z. Wang, A. J. Illingworth, E. J. O'Connor, W. B. Rossow, S. L. Durden, S. D. Miller, R. T. Austin, A. Benedetti, C. Mitrescu and the CloudSat Science Team, 2002: The CloudSat Mission and the A-Train. *Bull. Am. Meteorol. Soc.*, **83**, 1771–1790.
- van de Hulst, H. D., 1957: *Light scattering by small particles*. Wiley and sons, 470 pp.
- Winker, D. M., J. Pelon and M. P. McCormick, 2003: The CALIPSO mission: Spaceborne lidar for observation of aerosols and clouds. *Proc. SPIE*, **4893**, 1–11.
- Yang, P., K. N. Liou, K. Wyser and D. Mitchell, 2000: Parameterization of the scattering and absorption properties of individual ice crystals. *J. Geophys. Res.*, **105**, 4699–4718.